Pergamon

0301-9322(94)E0033-F

Int. J. Multiphase Flow Vol. 20, No. 4, pp. 671–689, 1994

0301-9322/94 $7.00 + 0.00

HEAT TRANSFER TO A LIQUID–SOLID MIXTURE IN A FLUME

G. HETSRONI and R. ROZENBLIT
Faculty of Mechanical Engineering, Technion—Israel Institute of Technology, Haifa, Israel

(Received 1 August 1993; in revised form 7 April 1994)

Abstract—Infrared thermography was used to study the thermal interaction between the particle-laden turbulent flow and a heated plate. Thermal streaks were observed on the heated plate, and the dimensionless mean distance Λ^+ between the streaks was found to increase with the Reynolds number. Introduction of polystyrene particles, within the uncertainty limits, did not change the value of Λ^+ in the flows with different particle volumetric loading Q_p/Q_o. Particles generally accumulated in the warmer regions of the heated plate, i.e. in the low velocity streaks.

The maximum amplitude of wall temperature fluctuations reached $\pm 40\%$ of the difference between the average wall temperature and the fluid bulk temperature. Consequently, there are variations in the heat transfer coefficient of the same order. The addition of particles changed the temperature fluctuations level. The location of the maximum of the dimensionless average heat transfer coefficient $\alpha_p/\alpha_o = f(Q_p/Q_o)$ depended on the Reynolds number and coincided with the location of the minimum non-dimensional RMS temperature fluctuation ratio, at the same Reynolds numbers.

Many of the experimental observations are presented here on an *ad hoc* basis, since we do not have, at this stage, a theory which can adequately describe the wealth of experimental observations.

Key Words: multiphase flow, heat transfer, wall temperature distribution, flume

1. INTRODUCTION

Here we study the heat transfer from a solid wall to liquid flowing in a flume. Since the coherent structures in the wall region have a dominant effect on the heat transfer, we also study these structures and examine the effect of solid particles on the structure of the turbulence in the wall region. Thus, through the effect of the particles on the coherent structure, we actually also examine the effect of particles on the heat transfer from a solid wall to a fluid.

The effect of the addition of solid particles on the heat transfer in turbulent flows has been the subject of many experimental investigations such as those of Jepson *et al.* (1963), Wilkinson & Norman (1967) and more recently of Hasegawa *et al.* (1983). The heat transfer from a tube or an array of tubes in suspension cross flow has been studied, e.g. by Murray & Fitzpatrick (1991), for a staggered array of tubes.

Plass & Molerus (1974) found that for a given suspension flow, the increase of heat transfer was strongly dependent on particle size. Later Zisselmar & Molerus (1979) showed that the solid particles increased or dampened the intensity of turbulence, depending on the concentration of solids as well as on the distance from the wall. They noted that the strongest increase in turbulence was observed in the same range of concentration of solids where the maximum heat transfer was achieved.

The problem of turbulence and particle interaction has two aspects: the dispersion of particles due to the turbulence of the carrier fluid, i.e. one-way coupling, and the modulation of the turbulence due to the presence of the particles, which is a two-way coupling between the turbulence and the particles. There have been a number of reviews on interaction between turbulence and particles without heat transfer between the wall and the fluid (e.g. Hetsroni 1989; Tsuji 1991). These will not be repeated here.

The streaky nature of the turbulent flow near a solid surface was first investigated by Boussinesq (1868). He experimented with air flow over a surface which was covered with coal powder in oil. Streaks on the oil indicated that low velocity and high velocity regions existed in the fluid. Much later, the streaky structure and coherent structures near the wall were made visible by flow

visualization techniques (Kline *et al.* 1967). The flow parallel to the wall forms low-speed and high-speed streaks that persist for very long distances. While these meander and shift around somewhat, the average spacing between the low speed streaks remains about $\Lambda^+ \cong 100[\Lambda^+ = \Lambda u^*/\nu$, where Λ is the distance between the streaks; $u^* = \sqrt{\tau/\rho}$ is the shear velocity, τ is the shear stress at the wall, ρ is the fluid density and ν is the fluid viscosity (Rashidi & Banerjee 1990; Rashidi *et al.* 1990)]. This dimensionless distance is remarkably resilient to changes in flow roughness, pressure gradient and other flow conditions. Kline *et al.* (1967) also presented evidence as to how these low velocity streaks lift up, oscillate and roll up into one or two ejections from the wall to the mainstream. These ejections, which cause the coherent structure to disappear, are called "bursts". Actually, the "bursting" phenomenon may occur due to horseshoe or hockeystick vortices which can be observed near the wall region in turbulent flow. The legs of these vortices are roughly aligned in the streamwise direction and their upper part is perpendicular to it. This upper part becomes unstable and is ejected from the wall region with the low velocity fluid. While the details of the process are not yet clear, they are well described elsewhere (e.g. Robinson 1991; Banerjee 1992).

Interaction of particles and coherent structures were reviewed by Rashidi *et al.* (1990). They state that "particulate matter suspended in the boundary layer interacts with the coherent structures, and that this interaction may be quite complex". Sumer & Deigaard (1981) made some measurements on the motion of 3.0 mm dia particles near a wall, using a photogrammetric system. They traced the motion of a single particle suspended in water in a horizontal channel. They found that, with a smooth bottom wall, the measured kinematical quantities characterizing the particle motion were in accord with available information on the bursting phenomena, as described above, suggesting that this is perhaps a mechanism to cause particle suspension in the flow. Dyer & Soulsby (1988) have similarly shown the importance of the bursting phenomenon on the transport of the particles on the ocean floor. The periodic ejection and in-sweep events associated with the bursting process have been captured in the instantaneous measurements of the Reynolds stress. This is seen as a sudden rise in the Reynolds stress magnitude of up to 30 times the mean Reynolds stress. In the ocean, these events are visible as swirls of sand that are lifted up above the ocean floor.

Rogers & Eaton (1989) measured the response of solid particles to a vertical turbulent boundary layer in air, using a low concentration of 50 and 90 μm glass particles. They found that the RMS velocity fluctuations of both particle sizes nearly equaled the streamwise turbulence intensity of the flow, but the turbulence intensity of the particles in the normal direction was strongly attenuated, i.e. much lower than the fluid's. The power spectra showed that for normal fluctuations the power spectrum shifts to higher frequencies relative to the streamwise fluctuations, therefore indicating that the particles did not closely follow the fluid fluctuations in the normal direction. Rogers and Eaton also used 70 μm copper particles to create a greater particle mass loading of 20%. The presence of these particles tended to suppress turbulence, with the degree of turbulence suppression being a function of the distance downstream in the boundary layer. They attributed the turbulence suppression to an increase in the dissipation. However, they were unable to clarify their results in light of the observed dominant flow events near the wall.

Yung *et al.* (1989) investigated the interaction between the turbulent bursts and the deposited particles within the viscous sublayer near the wall. They carefully placed spherical particles of polystyrene and glass (50 μm dia) on the wall so that the particles were completely submerged within the viscous sublayer. Their flow visualization experiments showed that the bursting phenomenon has an insignificant effect on re-entrainment of the deposited particles within the viscous layer. It was shown that only about 1% of the particles are lifted up into the flow by the wall bursts. However, as the size of the particles increased, the number of re-entrained particles also increased. Based on these results they concluded that, in contrast to the previous hypothesis, the turbulent bursts are not effective to re-entrain the particles within the experimental range of $0.5 < d^+ < 1.3$, where d^+ is the non-dimensional particle diameter ($=du^*/\nu$). On the other hand, as d^+ increased, the importance of turbulent bursts in particle re-entrainment substantially increased.

Cleaver & Yates (1973, 1975, 1976), in an attempt to model the particle transport in turbulent flows, suggested that the particles are re-entrained by the wall ejection events while they are deposited by the in-sweep events. Their model had some agreement with the limited experimental

data in predicting the particle deposition and re-entrainment rates. Although their model and some recent theoretical attempts have been based on some characteristics of the bursting phenomenon, there is still not enough experimental evidence as to the details of the turbulence–particle interactions for any realistic modeling of this problem.

Recently, the experimental investigation of a developing turbulent boundary layer over a heated flat plate was reported by Bagheri & White (1993). Space–time correlations of the temperature fluctuations t', mean convection velocity of the large-scale structure and isocorrelation contours were measured for three temperature differences between the wall and the free stream. In summary, it is suggested that the temperature fluctuation structures are more similar to the structure of the streamwise velocity fluctuations u' than the spanwise velocity fluctuations v' structure.

Heat transfer mechanisms and associated turbulence in the near-wall region of the turbulent boundary layer were studied by Iritani *et al.* (1983), for a single Reynolds number. They used a liquid crystal (LC) sheet, composed of 50 μm thick polyester, a liquid crystal layer and black paint. The total thickness was around 100 μm. They attached the LC sheet to a stainless steel foil, which was used as a heater, and which was glued to a bakelite plate. They showed that the temperature fluctuations had some similarity to the structure of the flow at the wall region. They estimated that the frequency response of their system is less than 2 Hz. This low response is due, in part, to the glue, polyester sheet and to the response of the LC itself.

Simonich & Moffat (1982) used gold deposited on polycarbonate in a water tunnel to study the turbulent boundary sublayer structure. This membrane was chosen to improve the frequency response of the surface. Analysis of the image shows (Moffat 1990) the sublayer streaky structure typical of a turbulent layer to represent amplitude variations in the heat transfer coefficient of about $\pm 15\%$ across the span of the image. They reported that at $\pm 25\%$ variation in heat transfer coefficient, their analytical solution predicted a frequency response of 3.5 Hz.

Our preliminary experiments with LC sheets yielded similar results, i.e. we estimated the frequency response of our system to be less than 3 Hz. We therefore decided not to use the LC techniques and to concentrate our effort on another technique, as described below.

2. EXPERIMENTAL

The objective of this study is to relate heat transfer to coherent structures and turbulence, and to examine the effect of particles on these.

2.1. Infrared thermography

The technique chosen for measuring the surface temperature was infrared thermography.

The temperature, as affected by the turbulent flow over the heater, was measured remotely by detecting infrared radiation from the heated surface in the range of 8–12 μm. For bodies at or near room temperature, the spectral energy distribution is such that the peak is in the middle of the infrared region, i.e. 10 μm. A sufficient amount of energy is radiated to allow calibration of this instrument in order to make highly accurate, non-contact, temperature measurements.

A high performance thermal imaging radiometer operates with one or a few individual detector signals scanned mechanically across the screen rather than with the large photosensitive surface typical of a TV camera. These detectors must be cooled to cryogenic temperatures. Nearly all systems incorporate scan conversion circuitry to create a TV compatible output.

Thermal imaging radiometers not only display an image of the temperature patterns radiating from the surfaces, but are also designed to produce temperature information as well. They also have a much faster response time (microsecond vs millisecond) than other thermometers (e.g. liquid crystals).

The Inframetrics Model 760 Infrared Thermal Imaging Radiometer† was used for the investigation of the thermal streaks pattern. It consists of a scanner and a control/electronics unit. The Model 760 scanner incorporates electromechanical servos to perform horizontal and vertical scanning. Horizontal scanning is performed at a 4 kHz rate in a resonant (sinusoidal) mode. Vertical scanning is done in a sawtooth pattern commensurate with standard TV formats. A

†This instrument was on loan from the manufacturer. This loan is gratefully acknowledged.

Mercury/Cadmium/Telluride detector is cooled by an integrated cooler to 77 K for maximum thermal sensitivity and high spatial resolution. The control/electronics unit contains circuits to process, digitize, reformat the IR signal for display in color or black and white on the display or external video monitor.

The temperature range of the Inframetrics Model 760 is -20 to 1500°C, with a minimum detectable temperature difference of 0.1°C at 30°C. Through calibration, the thermal imaging radiometer is very accurate in a narrow temperature range giving typical noise equivalent temperature difference (NETD) only, which is less than 0.2°C (with image average less than 0.05°C). A typical horizontal resolution 1.8 mRad or 256 pixels/line.

For all of the performance characteristics mentioned above, it is assumed that the surface of the heater behaves as a black body ($\epsilon = 1$). In most concrete cases, the emissivity of the model surface is less than unity (in particular, with metal models). To avoid an additional error in emittance measurement, the heater was coated with paint which is "black" in the infrared range.

A reference color bar is displayed on the bottom portion of the color monitor screen. It is possible to choose from eight color palettes (up to 20 colors). The Line Select mode allows one to choose a horizontal cursor to obtain a quantitative temperature graph. In addition, there is a Fast-Line Scan mode to analyze events at 125 μs intervals. A mode Area displays the average temperature at the region within the user-defined box.

Some good results have been obtained in the last few years in measurements of the convective heat transfer and the flow field visualization by means of infrared thermography (e.g. Gauffre 1988; Giovanni 1993). Due to the high frequency response of this technique (see appendix) and its precision, we decided to use it, as described below.

2.2. The experimental facility

The flume is a stainless steel channel made of three sections and overall is 4.3 m long, 0.32 m wide and 0.1 m deep (figure 1). The flow is produced by a centrifugal pump and is measured by means of a flowmeter. The recirculating water is filtered continuously to remove solids larger than 5 μm. Measurements of the liquid temperature are made at the entrance and exit of the channel, using precision mercury thermometers placed in the water. Great care was taken to eliminate wave formation at the inlet and reflections from the outlet. Effort was also made to maintain a constant average velocity and temperature throughout each run.

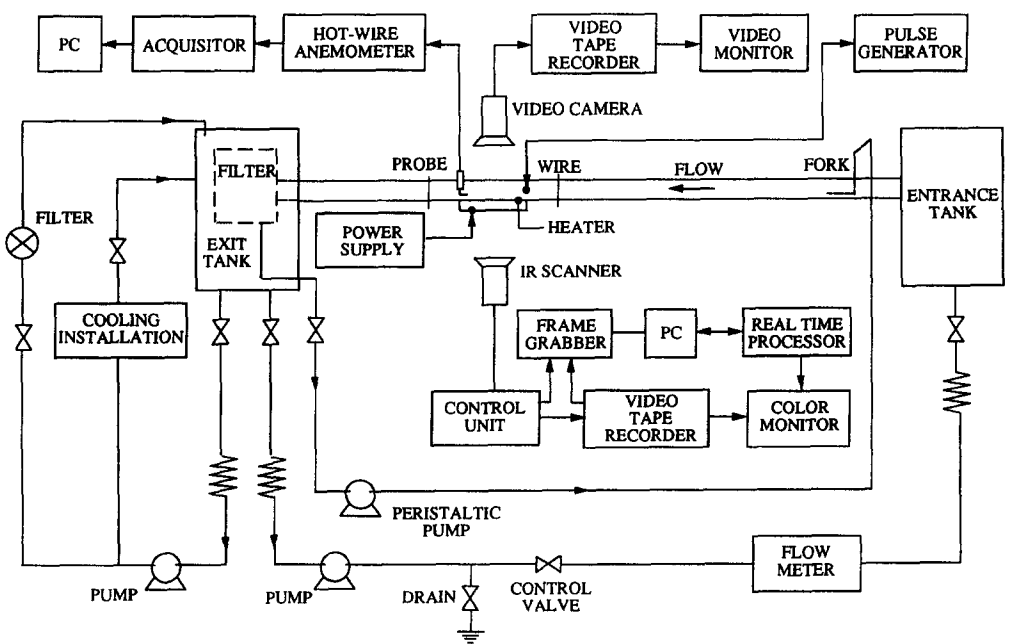

Figure 1. Schematic diagram of the experimental facility.

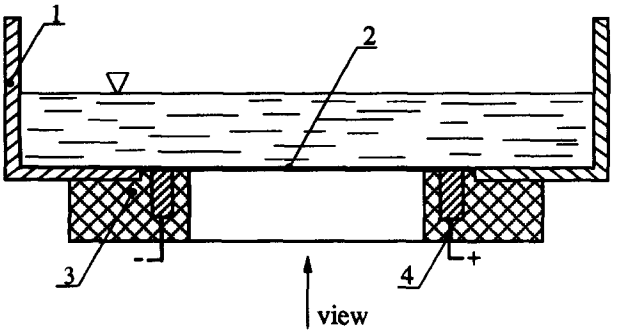

Figure 2. Test section for the infrared visualization. 1, Channel; 2, constantan heater; 3, frame; 4, contacts.

The constantan heater is located at the bottom of the test section (figure 2). It is a strained foil which is 0.33 m long, 0.20 m wide and 50 μm thick. The straining mechanism allows the foil to be "pulled" on an isolated frame without visible surface distortion. There is a window in the central zone of the frame which is 0.30 m long and 0.15 m wide. The foil is attached to the window by means of contact adhesive and is coated on the bottom (i.e. not on the water side) with black matt paint of about 20 μm thickness. Constant heat flux is achieved by supplying D.C. power up to 300 A.

Wall temperature measurement and non-stationary temperature distribution are measured by using the IR imaging radiometer described above. In addition, the hydrogen bubble method was used for flow visualization. The bubbles were produced by applying electric pulses (10–80 pulse s^{-1} with a pulse duration of 5–20 ms and a voltage up to 350 V), on a horizontal wire which was suspended at a distance of 0.12 m from the leading edge of the heater, and could be moved up and down between the bottom of the flume and the interface. The uncertainty in the vertical location of the wire is $\delta y^+ \leqslant 1.0$ ($y^+ = yu^*/\nu$ is the dimensionless distance from the wall, y is the distance from the wall). Two-dimensional non-stationary hydrogen bubble distribution was recorded by means of a S-VHS video camera. In these experiments, data were generally recorded at 50 frames s^{-1}.

The polystyrene particles are introduced in the flow at about 2.2 m upstream from the test section. This is done (for particles up to $d_p \leqslant 1$ mm) by using a fork made of two tubings, 4 mm in dia, placed in the center of the channel. The particle solution is introduced into the flow by a variable-speed peristaltic pump, in such a way that the particles are added to the flow with a known concentration and flow rate. A jet pump is used to introduce larger particles of diameter $\bar{d}_p = 3.2$ mm into the flow. The concentration uniformity in the span-wise direction is checked by visual observation. A particle distribution in a similar channel as a function of the dimensionless distance from the wall was studied by Rashidi *et al.* (1990) and Kaftori *et al.* (1992, 1994).

The added particles were collected at the exit of the channel by using a cylindrical funnel of 0.40 m dia and of 0.45 m length made of porous material. The particle loading was controlled by changing either the solution concentration in the filter or the pump speed.

2.3. Experimental conditions and procedures

In an experimental run the desired thermal and flow conditions were established first. Since we used joule heating, we set the heat flux, and the temperature was determined by the system. It is best to have an average wall temperature of about 30°C, which is the peak of the energy spectrum at a wavelength of about 10 μm.

The temperature distribution, average and fluctuating temperatures were measured using the IR imaging radiometer. The scanner of the IR radiometer was situated *under* the heater plate at a distance of about 0.5 m. Both the uniformity of the temperature field of the heater and the noise equivalent temperature difference (NETD) were estimated at the heater surface temperature (within the experimental range 25 ~ 30°C). These were carried out both with stagnant warm water and without water in the flume. The common uncertainty (spatial and temporal) did not exceed 0.15°C. The uncertainty was determined by comparing the IR radiometer indications with a precision mercury thermometer placed in the water.

Table 1. Flow conditions

Mean velocity, U_M (cm s^{-1})	Mean temperature of water, t_L (°C)	Flow depth, h (cm)	Reynolds number $Re_h = \frac{U_M \cdot h}{\nu}$	Friction velocity, u^* (cm s^{-1})	Heat flux, q (W cm^{-2})	Reynolds number, Re_D $Re_D = \frac{U_M \cdot D}{\nu}$
14.1	20 ± 0.2	3.7	5100	0.81	1.01	16,500
16.5	20	3.7	6000	0.93	1.01	19,500
18.8	20	3.7	6800	1.04	1.01	22,100
21.2	20	3.7	7700	1.16	1.01	25,000
23.5	20	3.7	8500	1.27	1.01	27,500
25.9	20	3.7	9400	1.38	1.01	30,500
28.2	20	3.7	10,250	1.49	1.01	33,200
28.2	38.5	3.7	15,400	1.41	1.01	50,000

Each run was carried out both with particles and without particles. Table 1 lists some typical hydrodynamic and thermal parameters at the measurement stations. Particle characteristics are listed in table 2.

The IR scanner was used to observe the change of thermal pattern, the temperature average at the central zone of the heater, the temperature distribution (i.e. the thermal streaks), as well as in Fast-Line Scan mode to analyze the data of a temperature graph at 125 μs intervals. Simultaneously, a thermal pattern was saved on a diskette and a video cassette. The video was then used in a playback mode to analyze the data, i.e. to freeze quantitative temperature graphs at a typical flow condition on the TV monitor, and to count the number of thermal streaks on the screen, and thus determine the average distance Λ between the streaks. The temperature distribution was also used for an estimate of the RMS temperature fluctuations. The data of average temperature at a central zone of the heater were used for the heat transfer coefficient definition.

The mean streamwise velocity profile was measured using hot-film anemometry. A hot film anemometer with a standard single-sensor boundary-layer probe was used for mean profile measurements. The probe was connected to a transversing mechanism having a spatial resolution of 10 μm. The anemometer signal was transmitted in digital code through an acquisitor to a PC. The hot-film probe was calibrated in the water flume by means of a hydrogen bubble flow visualization technique (e.g. Rashidi & Banerjee 1988). The streamwise velocity profiles obtained were then employed to ascertain that the flow is hydraulically fully developed at the heater, and to determine values of the friction velocity u^*, by means of "Clauser-type" fits. These measurements were carried out to confirm the use in our case of either the Blasius equation $u^* = 0.167 U_M Re_h^{-0.125}$ (applied under similar conditions by Rashidi & Banerjee 1988) or $u^* = U_M \cdot (64.53 Re_h^{-1} + 0.046)$ which was measured by Kaftori (1993) in an identical flume (here U_M is the mean velocity and $Re_h = U_M h/\nu$, where h is the water level). Comparison of the values revealed that both equations gave satisfactory results in the range of Reynolds numbers used. According to Kaftori (1993), the presence of particles increased u^* by 1–6% at comparable Reynolds numbers, with the exception of the small (100 and 275 μm) particles at $Re_h = 14{,}000$, where u^* was reduced by approx. 1–3%. He noted also, that the particle concentration has no significant effect.

The streaky structure in the water was observed by means of hydrogen bubble-wire tracers. This visualization technique was used before for various experimental conditions (e.g. Kline *et al.* 1967; Smith & Metzler 1983; Rashidi & Banerjee 1988). Their results indicated that the dimensionless spanwise streak spacing was essentially invariant with the Reynolds number, exhibiting consistent values of $\Lambda^+ = 100 \pm 20$. Further studies showed that Λ^+ was approximately constant in the very-near-wall region ($y^+ \leqslant 5$). For $y^+ \geqslant 10$, Λ^+ increased with increasing y^+.

Table 2. Particle characteristics

Particle type	Diameter (mm)	Specific gravity (g cm^{-3})	Particle geometry	Volumetric loading $Q_p/Q_o \times 10^4$
Polystyrene	0.92 ± 0.08	1.03 ± 0.02	spherical	0.4–6.2
Polystyrene	0.33	1.03	spherical	0.4–0.7
Polyethylene high density	3.2	1.25	spherical	0.6–17.6

Table 3. Typical uncertainty estimates

Variable	Uncertainty
t_L	0.05°C
t_W	0.15°C
$\bar{t}_w$	0.05°C
U_M	2%
u^*	5.5%
h	0.8%
Re_h	2.4%
q	1.1%
Λ^+	9.2%
Q_p/Q_o	1.8%

The video camera was placed at about 1.5 m above the flume. A light beam was introduced into the water through glass windows, on the lateral walls of the flume. Bubble tracers were recorded by means of a video camera. The time of recording was about 150 s for each run. The video tape was then used to analyze the data in a similar manner that was used for the temperatures. The uncertainty caused by equipment inaccuracy and statistical variations was estimated. In each run at least 30 frames (Kline *et al.* 1967) were counted to reach the mean distance between the streaks both in temperature graphs and in bubble tracer runs. Typical uncertainty estimates are listed in table 3.

3. EXPERIMENTAL RESULTS

3.1. Clear fluid

The IR image of the heater was recorded from below, i.e. not on the water side. Since the heater is very thin (only 50 μm), and has almost no thermal inertia, it is assumed that this temperature pattern is very similar to the temperature on the other side, i.e. the temperature which we measure is almost the same as the temperature at the bottom of the flume, at $y^+ = 0$, and there is a non-significant temperature discrepancy of the mean temperatures of the two heater sides of about 0.12°C (see appendix).

Figure 3 illustrates the temperature structure on the wall, depending on the Reynolds number, without particles. The color shades are proportional to the temperatures, and thus reveal the streaky structure of the temperature on the wall. These thermal streaks are quite long and resilient, though they meander about somewhat.

A more quantitative picture of the temperature distribution across the heater in the spanwise direction at the middle of the heater is given in figure 4.

During each run a sequency of at least 150 s was recorded. From this sequence, 30 frames were analyzed. Both the width of the spanwise-streak spacing and the RMS temperature fluctuations within the spanwise streak-spacing were examined. Each temperature curve depicts a succession of peaks. The mean distance between adjacent maxima was used to estimate Λ^+. We neglected fluctuations having an amplitude of less than the RMS value of the temperature fluctuations.

The data were also processed in a different way: the image of thermal streaks (after reducing noise through convolution by Gaussian type filters) represents a graph of grey levels from 0 to 256 units versus the spanwise coordinate (0–300). The grey levels graph shows clear peaks (figure 5). The mean number of peaks per frame (neglecting the fluctuations having small value), were counted, and agreed with the number of peaks in figure 4.

3.2. Fluid–particles mixture

The wall temperature distribution when a fluid–particles mixture was flowing in the flume, is depicted in figure 6, for two values of particle loading (Q_p is the volumetric flow rate of the particles and Q_o is the volumetric flow rate of the fluid).

In figure 7 the particles are observed to accumulate in the warmer region, i.e. in the region of low velocity. (This photograph was taken with the heater covered with a liquid crystal sheet. The blue indicates the higher temperature.)

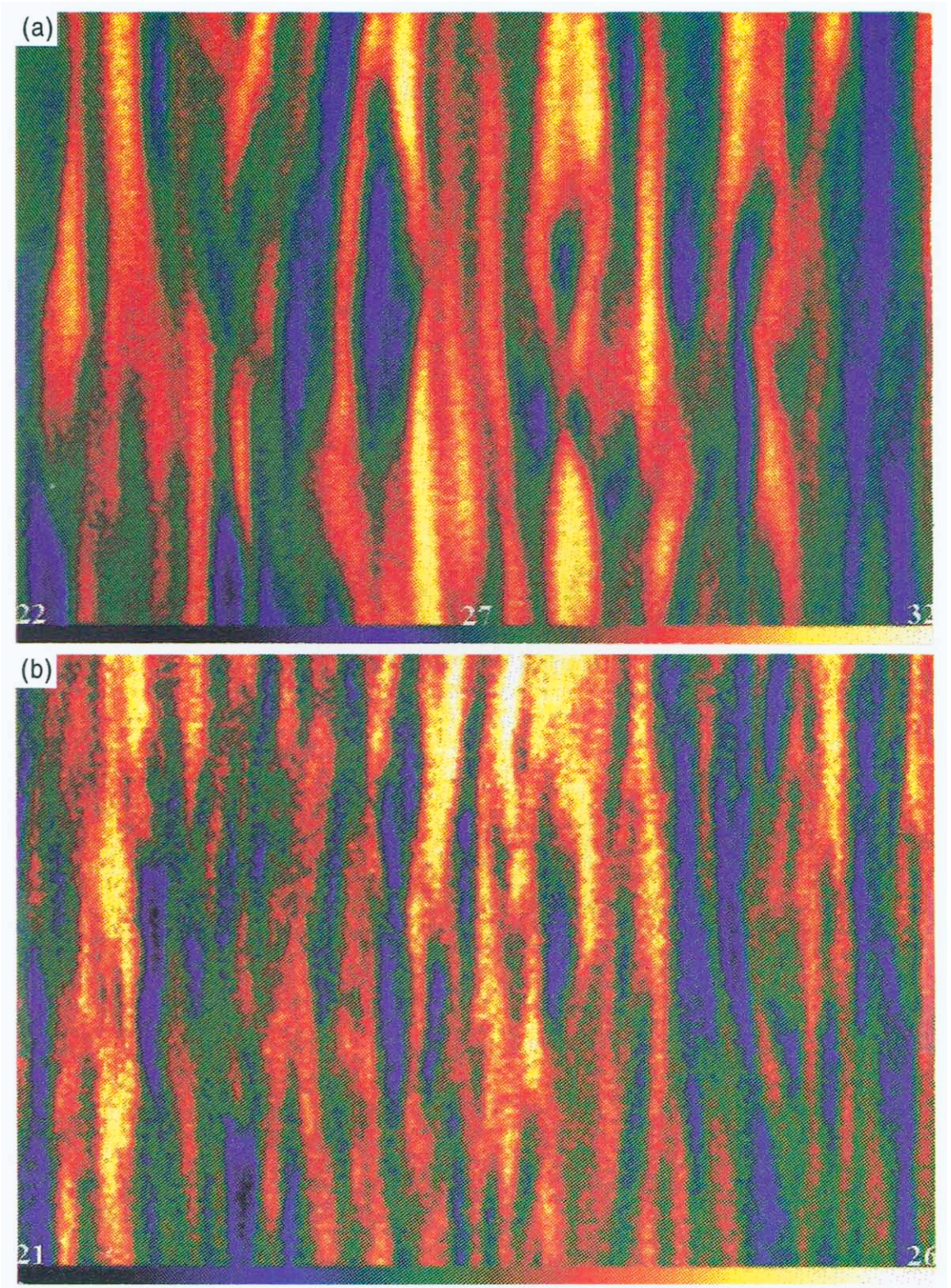

Figure 3. Change of temperature structure near the wall, depending on the Reynolds number (IR image), clear fluid. (a) $Re_h = 5100$; (b) $Re_h = 9400$. Flow direction is from the bottom to the top. The color play interval is: (a) 10°C; (b) 5°C. Dimensionless width of the figure is: (a) $\Delta z^+ = 1170$; (b) $\Delta z^+ = 1990$.

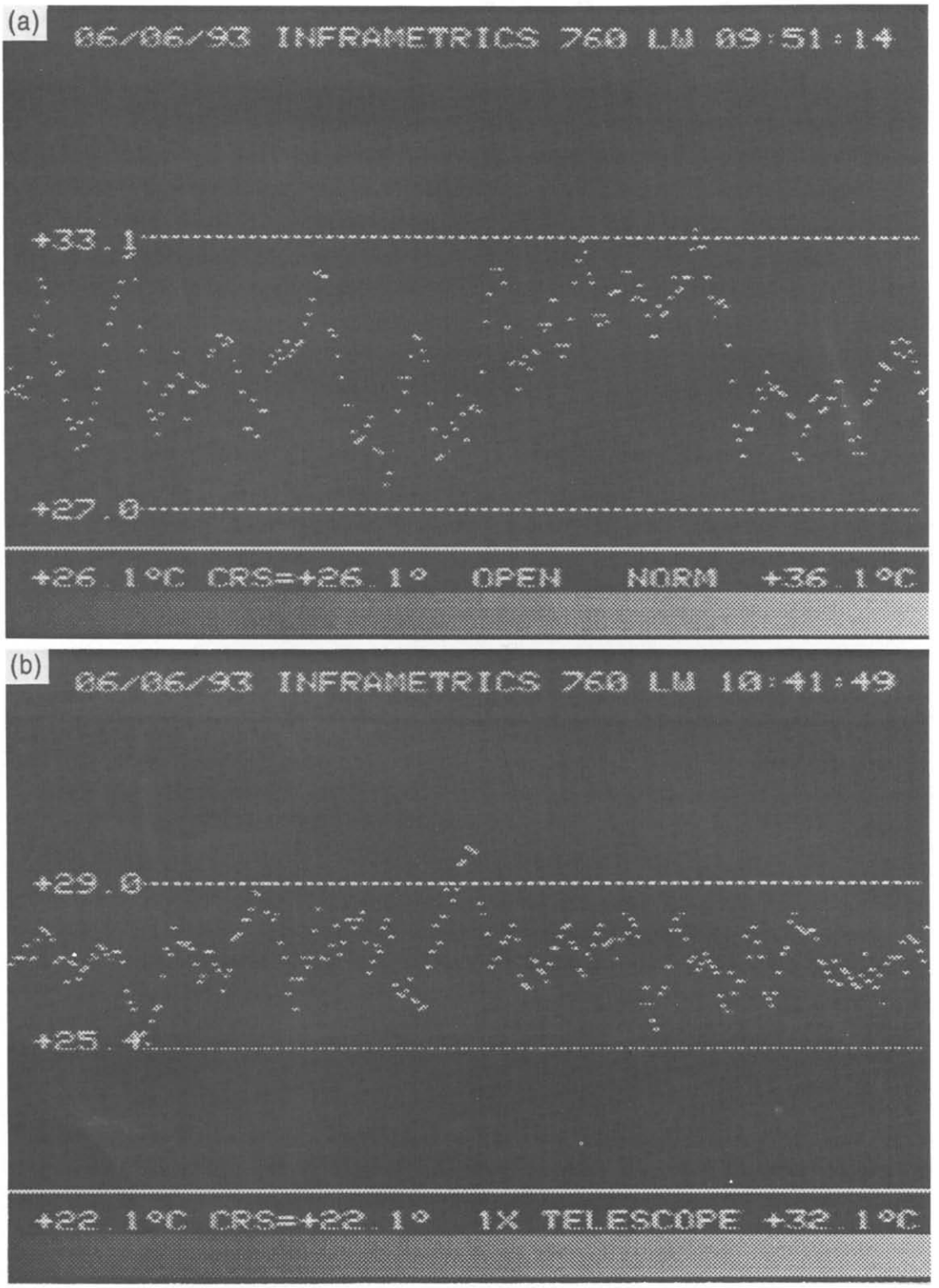

Figure 4. Quantitative temperature curves. (a) $Re_h = 5100$; (b) $Re_h = 7700$. The points are instantaneous temperatures along the spanwise direction. The dotted lines are an approximate dynamic interval of the temperature fluctuations. Dimensionless width of the figure is: (a) $\Delta z^+ = 1170$; (b) $\Delta z^+ = 1670$.

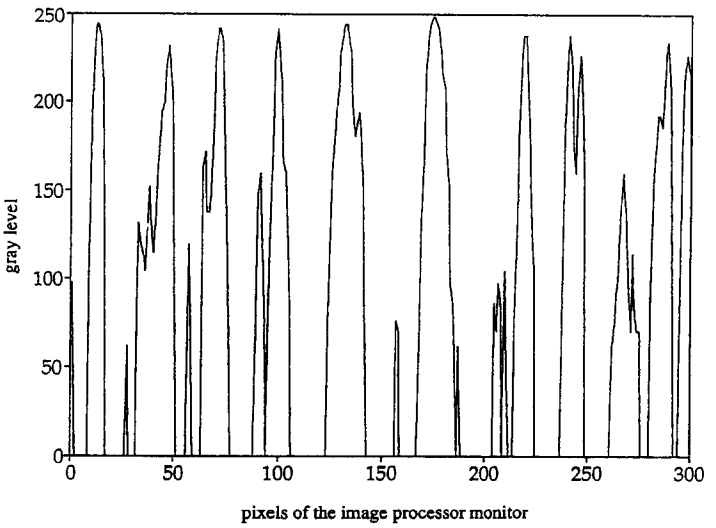

Figure 5. An image fragment (300 out of 512 pixels) of the thermal streaks in the form of the gray level graph along the spanwise direction.

It is clear from the figure that the addition of the particles has a profound effect on the structure of the streaks in the wall region. Thusfar, this is only a visual observation and we were not able to quantify or explain it.

Figure 8 shows the variation of the mean dimensionless, spanwise thermal streak-spacing, $\Lambda^+ = \Lambda u^*/\nu$ as a function of the Reynolds number, based on the flow depth $h(\mathrm{Re}_h = U_M h/\nu)$. As seen from figure 8, the mean dimensionless spanwise thermal streak-spacing increases with Re_h, in the range of Reynolds numbers investigated here. This observation is true for clear liquid, as well as for a liquid–particles mixture. The loading of the particles has some small effect on the spacing.

We also measured the low velocity streaks by means of the microbubbles technique. Figure 9 depicts the dimensionless streak spacing versus the dimensionless height from the bottom of the flume $y^+(y^+ = yu^*/\nu$, where y is the distance from the bottom of the flume). The value of Λ^+ at $\mathrm{Re}_h = 7500$ with the heater on and also with the heater off, are shown on this graph. The value of Λ^+ of the thermal streak is at $y^+ = 0$. Though the data points with the heater on are higher than the data points with the heater off, the difference between them is not (statistically) significant. The variation of the mean dimensionless spanwise streak-spacing, as a function of the distance from the wall, $\Lambda^+ = f(y^+)$, generally agrees with the results of other studies (e.g. Smith & Metzler 1983).

Our results are compared to those of various other measuring techniques in table 4. It should be noted that the values of Λ^+ in this study are somewhat lower than the mean value. This may be due to our relatively low Reynolds numbers.

The root-mean-square (RMS) wall temperature fluctuation t_o^{RMS} generally had a value of 9–12% of the difference between the temperatures of the wall and the bulk of the liquid without particles. In some cases, however, maximum temperature fluctuations reached an amplitude as high as $\pm 40\%$. Namely, there are variations of the heat transfer coefficient of the same order. The addition of particles to the flow changes the temperature fluctuation level. Actually, at low Reynolds numbers and heavy particle loading, the temperature difference *between* the streaks on the wall can exceed the difference between the bulk temperature of the fluid and the average temperature of the wall.

In figure 10 is shown the ratio of the dimensionless RMS values of temperature fluctuation t'_p/t'_o versus particle loading at three values of the Reynolds number $[t'_p = t_p^{\mathrm{RMS}}/(\bar{t}_p - t_L)$ is the dimensionless RMS temperature fluctuation on the wall for flow with particles, and $t'_o/(\bar{t} - t_L)$ is the dimensionless RMS wall temperature fluctuation with clear fluid, $\bar{t}_p$ is the area-average temperature of the wall with particles, $\bar{t}$ is the area-average temperature of the wall with clear fluid and t_L is the liquid bulk temperature].

Two out of three curves have somewhat fuzzy minima.

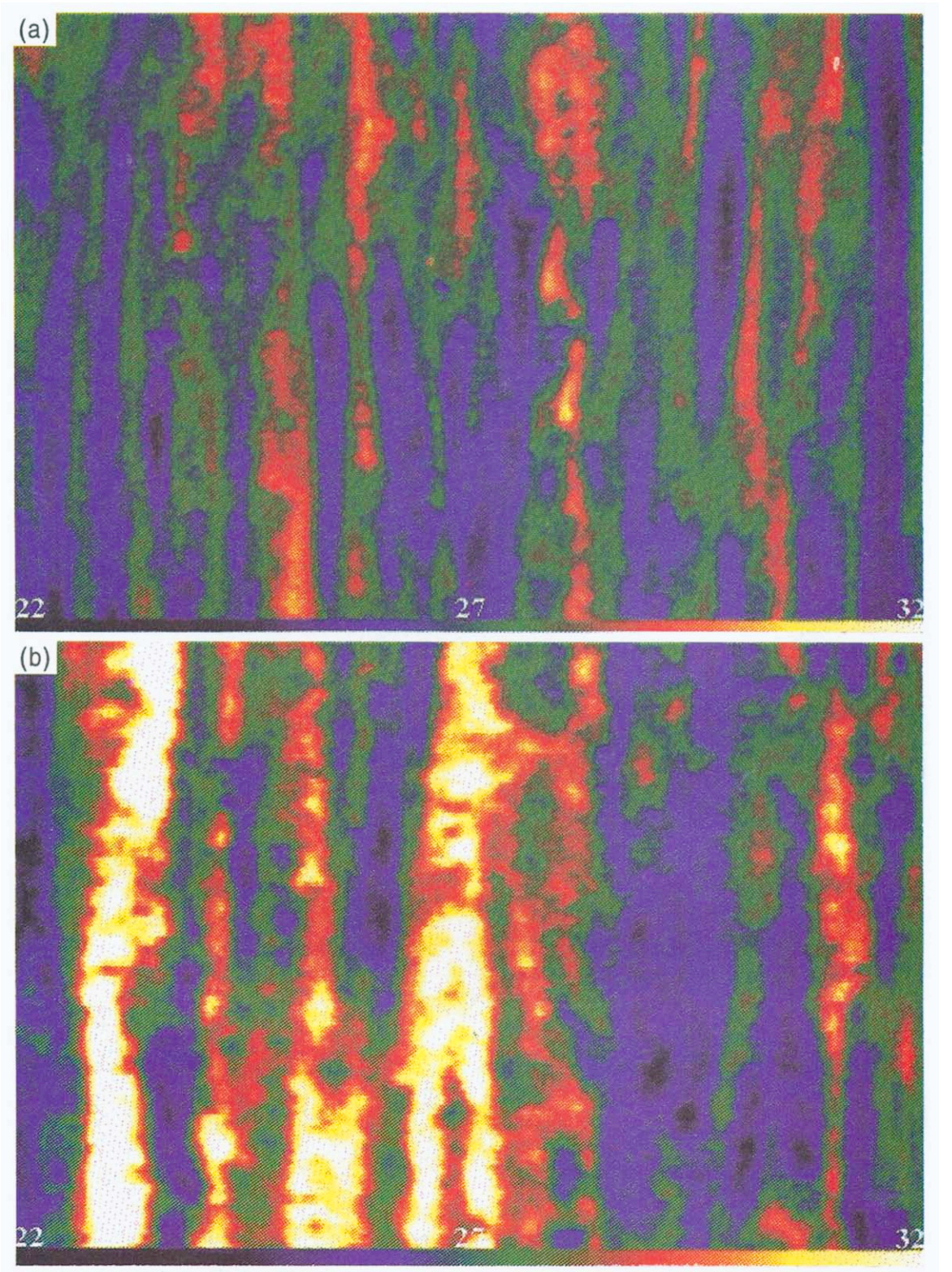

Figure 6. Change of the structure near the wall, depending on the Reynolds number with particles (IR image). (a) $Re_h = 5100$, $Q_p/Q_o = 1.5 \times 10^{-4}$, $d_p = 0.92$ mm; (b) $Re_h = 5100$, $Q_p/Q_o = 3.5 \times 10^{-4}$, $d_p = 0.92$ mm. Flow direction is from the bottom to the top. The color play interval is 10°C. Dimensionless width of the figure is $\Delta z^+ = 1170$.

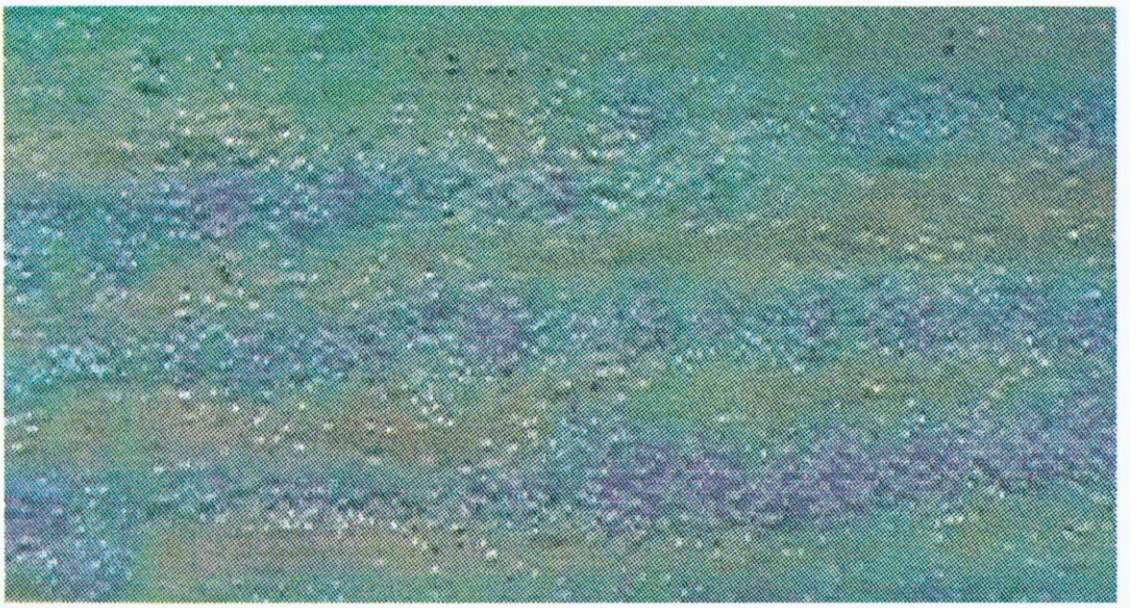

Figure 7. Particles, $d_p = 0.92$ mm, accumulate in the low velocity, higher temperature, regions.

3.3. *Heat transfer coefficient*

As stated above, one of the objectives of this study was to determine the variation of the heat transfer coefficient from the wall to the fluid, and to study the effect of addition of particles to the fluid on the heat transfer coefficient.

For the definition of the dimensionless average heat transfer coefficient, we used the average temperature at the center of the heater (10 cm in streamwise and 14.4 cm in spanwise directions). The measurements were carried out in the mode "Area" of the IR radiometer, both with and without the particles.

The relative average heat transfer coefficient is defined as

$$\alpha_p/\alpha_o = (\bar{t} - t_L)/(\bar{t}_p - t_L) \quad [1]$$

Here α_p is the heat transfer coefficient (wall to fluid) when particles are present, α_o is the heat transfer coefficient for clear fluid, $\bar{t}$ is the area-average temperature of the wall with clear fluid, $\bar{t}_p$ is the area-average temperature of the wall with particles and t_L is the liquid bulk temperature.

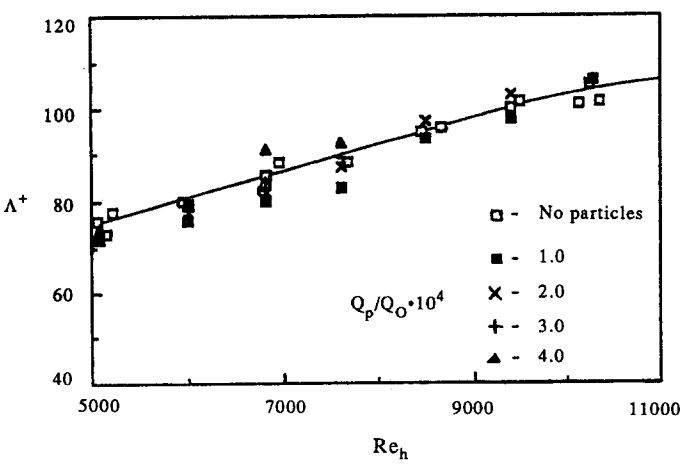

Figure 8. Variation of the mean dimensionless spanwise thermal streak-spacing as a function of the Reynolds number at different particle loading, Q_p/Q_o.

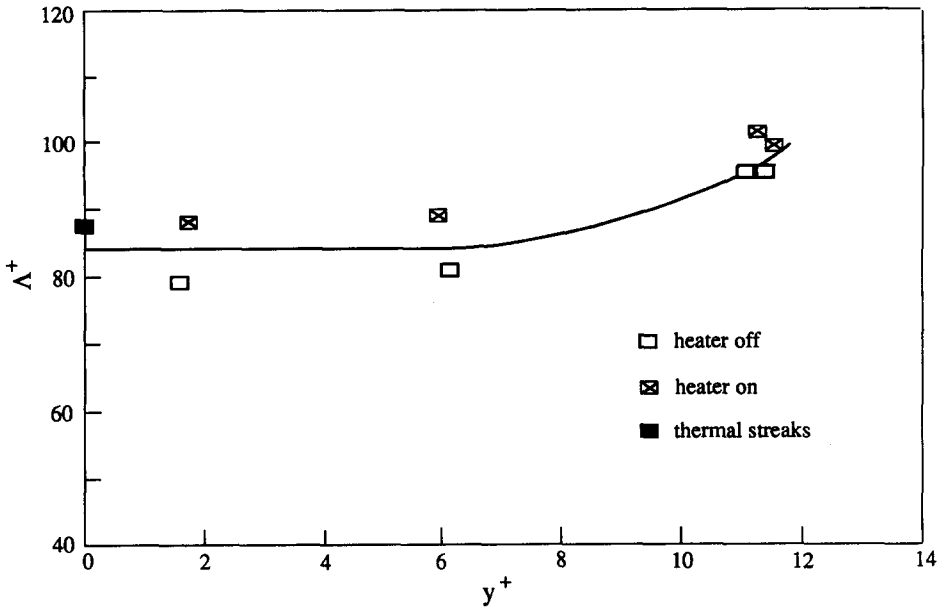

Figure 9. Variation of the mean dimensionless spanwise streak-spacing Λ^+ as a function of the dimensionless height y^+ from the bottom of the flume, $Re_h = 7500$; no particles.

Figure 11 depicts the variation of the value α_p/α_o as a function of the particle loading Q_p/Q_o at different Reynolds numbers Re_h. The curves display maxima, with the location of each maximum depending on the Reynolds number. It should be noted, that the location of the maximum of the dimensionless average heat transfer coefficient coincides with the location of the minimum of the dimensionless RMS temperature fluctuation ratio. It should also be noted that Zisselmar & Molerus (1979) observed the strongest increase in turbulence in the same range of solid concentration in which maximum heat transfer is achieved.

It can be seen that the maxima are shifted to the right with the increase of Re_h. For $Re_h > 6800$ we could not reach a maximum, since an increase in loading did not increase the heat transfer but caused a build up of particle dunes on the bottom of the flume.

3.4. Large particles

Finally, we also studied the effect of large particles on the wall temperature and on the heat transfer coefficient. We used high density polyethylene, specific gravity 1.25, of 3.2 mm dia (though the particles were not perfectly spherical).

Figure 12 shows the variation of the dimensionless average heat transfer coefficient α_p/α_o as a function of the particle loading Q_p/Q_o. The heat transfer coefficient also increases with the particle loading. However, in contrast to the smaller particles where the dunes meander in the streamwise direction, at a high loading of large particles, dunes which are formed on the bottom, do not move.

Table 4. Comparative results of various methods of Λ^+ definition

Method	U_∞ (U_M) ($m\,s^{-1}$)	Re_θ (Re_D)	Λ^+	Reference
Dye, channel flow	0.06–0.229	2060	67	Kline *et al.* (1967)
	0.169–0.335	298–480	88–108	Oldaker & Tiederman (1977)
Hologram, interferometry, pipe flow	0.249–0.553	327–725	79–93	Achia & Thompson (1976)
Liquid crystal, closed-loop channel	0.204	990	81	Iritani *et al.* (1983)
Thermography, open channel	(0.141–0.282)	(16500–33200)	73–104	This study
Hydrogen bubbles, $y^+ = 4 \div 10$	—	$(2 \times 10^5 + 8 \times 10^5)$	100 ± 20	Kim *et al.* (1971)
	0.121–0.582	740–5830	$87 \div 104$	Smith & Metzler (1983)

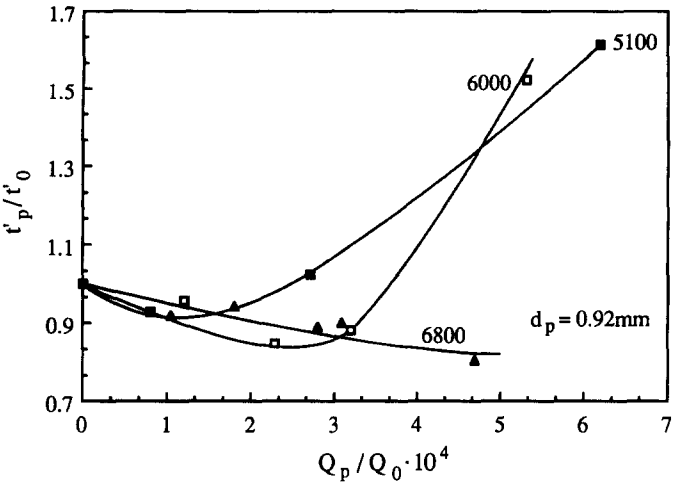

Figure 10. Ratio of the dimensionless values of the RMS temperature fluctuations t'_p/t'_0 vs the particle loading at three Reynolds numbers.

4. SUMMARY AND DISCUSSION

The IR technique was shown to be an effective means to study patterns of wall temperature and how these are affected by velocity streaks and coherent structures. It has been demonstrated to be a non-intrusive, fast-response and high-resolution method for measuring temperature distributions on solid surfaces. Since water is opaque to IR wavelength, we proposed a heater with a very low response time which enabled us to carry out these measurements from the bottom.

These measurements, together with flow visualization, revealed a streaky structure on the heated plate in a hydraulically fully developed flow in a water flume. The mean dimensionless distance between the streaks was found to increase with the Reynolds number. The thermal streaks seem to correspond to the velocity streaks, i.e. the high temperature lines seem to be the low velocity streaks on the surface. The introduction of particles, within the limits of uncertainty, did not change the value of Λ^+ in the flows with different particle loading.

The particles generally accumulated in the warmer regions of the heated plate, i.e. in the low-speed regions as observed by Kaftori *et al.* (1994) and computed by Pedinotti *et al.* (1992). Larger particles were uniformly distributed and did not accumulate in streaks.

The root mean square temperature fluctuations on the heated wall reached 9–12% of the difference between the bulk temperature of the clear fluid and of the average wall temperature. However, we noted that maximum wall temperature amplitude fluctuations reached $\pm 40\%$.

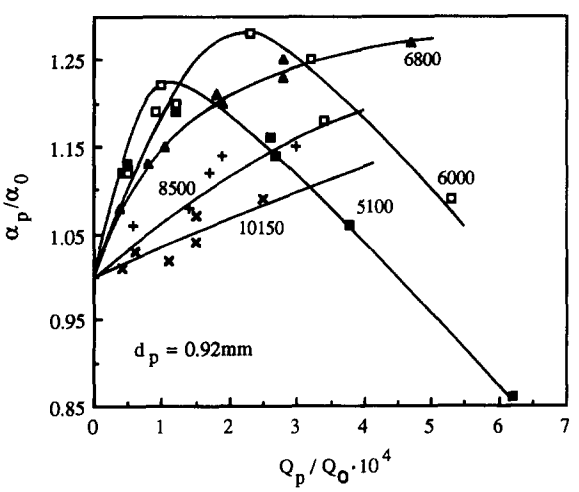

Figure 11. Variation of the average dimensionless heat transfer coefficient α_p/α_0 as a function of the particle loading Q_p/Q_0 at different Reynolds numbers Re_h ($d_p = 0.92$ mm).

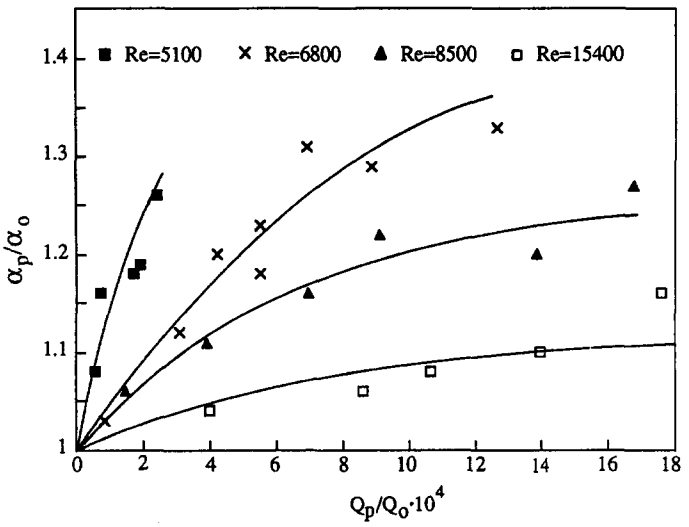

Figure 12. Variation of the average dimensionless heat transfer coefficient α_p/α_o as a function of the particle loading Q_p/Q_o at different Reynolds numbers Re_h ($d_p = 3.2$ mm).

Consequently, there are variations of the same order in the local non-steady-state heat transfer coefficient. The addition of particles to the flow changed the temperature fluctuation level. The wall temperature difference between the streaks can actually exceed the difference between the average wall temperature and the bulk temperature of the fluid, at low Reynolds numbers and high particle loading.

For the polystyrene particles of $d_p = 0.92$ mm, there are maxima of the dimensionless average heat transfer coefficient α_p/α_o. The maximum location of each curve $\alpha_p/\alpha_o = f(Q_p/Q_o)$ depends on the Reynolds number and coincides with the location of the minimum dimensionless RMS temperature fluctuation ratio, at comparable Reynolds numbers.

A few experiments with the polystyrene particles of $d_p = 0.33$ mm showed that the dimensionless heat transfer coefficient α_p/α_o varies with the limits $\pm 5\%$ at $Q_p/Q_o = 0.3 \div 0.7 \times 10^{-4}$.

Thus, it may be assumed that large polymer particles (0.92 and 3.2 mm) cause an increase in heat transfer coefficient, whereas smaller particles (0.33 mm) bring about an insignificant increase or even a decrease of the average dimensionless heat transfer coefficient. These results are in good agreement with the results of Rashidi *et al.* (1990), which show that the larger polystyrene particles ($d_p = 1100\ \mu$m) cause an increase in the number of wall ejections giving rise to an increase in the measured values of the turbulence intensities and Reynolds stresses. On the other hand, the smaller polystyrene particles ($d_p = 120\ \mu$m) caused a decrease in the number of wall ejections causing a decrease in the measured intensities and Reynolds stresses, for a Reynolds number of the order of 5000.

Finally, there are many unresolved issues, e.g. the high temperature streaks affect the temperature of the water in the flume and thus reduce the kinematic viscosity—how does this affect the structure of the flow near the wall?; it is not clear exactly how the particles increase the heat transfer coefficient, etc.

Acknowledgements—This research was supported by a United States–Israel Binational Science Foundation Grant #90-00428/1, by the Technion VPR Fund–Israel–Mexico Energy Research Fund, and by the Fund for the Promotion of Research at the Technion. RR is partially supported by the Center for Absorption in Science, Ministry of Immigrants Absorption, State of Israel.

REFERENCES

ACHIA, B. U. & THOMPSON, D. W. 1976 Structure of the turbulent boundary in drag-reducing pipe flow. *J. Fluid Mech.* **81,** 439–464.

BAGHERI, N. & WHITE, B. R. 1993 Experimental measurement of large-scale temperature fluctuations structures in a heated incompressible turbulent boundary layer. *Int. J. Heat Mass Transfer* **36,** 907–918.

BANERJEE, S. 1992 Turbulence structure. *Chem. Engng. Sci.* **47,** 1793–1817.

BOUSSINESQ, 1868 Memoire sur l'influence des frottements dans les mouvements reguliers des fluides. *J. Math. Pures Appl.*

CLEAVER, J. W. & YATES, B. 1973 Mechanism detachment of colloid particles from a flat substrate in turbulent flow. *J. Colloid Interface Sci.* **44,** 464–473.

CLEAVER, J. W. & YATES, B. 1975 A sublayer model for deposition of the particles from turbulent flow. *Chem. Engng Sci.* **30,** 983–992.

CLEAVER, J. W. & YATES, B. 1976 The effect of re-entrainment on particle deposition. *Chem. Engng Sci.* **31,** 147–151.

DYER, K. R. & SOULSBY, R. L. 1988 Sand transport on the continental shelf. *A. Rev. Fluid Mech.* **210,** 295–324.

GAUFFRE G. 1988 Detection of laminar-turbulent transition by infrared thermography. *La Recherche Aerospatiale* **2,** 11–22.

GIOVANNI, M. C. 1993 Flow visualization and convective heat transfer measurements by means of infrared thermography. In *Imaging in Transport Processes* (Edited by SIDEMEN, S. & HIJIKATA, K.), pp. 97–108. Begell House, New York.

HASEGAWA, S., ECHIGO, R., KANEMARU, K., ICHIMIYA, K. & SANUI, M. 1983 Experimental study of forced convective heat transfer of flowing gaseous solid suspension at high temperature. *Int. J. Multiphase Flow* **9,** 131–145.

HETSRONI, G. 1989 Particle–turbulence interaction. *Int. J. Multiphase Flow* **15,** 735–746.

IRITANI, Y., KASAGI, N. & HIRATA, M. 1983 Heat transfer mechanism and associated turbulence structure in the near-wall region of a turbulent boundary layer. *Turbulent Shear Flows* **IV,** 223–234.

JEPSON, G., POLL, A. & SMITH, W. 1963 Heat transfer from gas to wall in a gas–solids transport line. *Trans. Inst. Chem. Engng* **41,** 207–211.

KAFTORI, D. 1993 Structure in the turbulent boundary layer and their interaction with particles. Ph.D. thesis, University of California, Santa Barbara, CA.

KAFTORI, D., HETSRONI, G. & BANERJEE, S. 1992 Modulation of turbulence structures by particles. *AIChE Meeting*, 1–6 Nov., Miami, FL.

KAFTORI, D., HETSRONI, G. & BANERJEE, S. 1994 Funnel-shaped vortical structures in wall turbulence. Accepted for publication in *Phys. Fluids A.*

KIM, H. T., KLINE, S. J. & REYNOLDS, W. C. 1971 The production of turbulence near a smooth wall in a turbulent boundary layer. *J. Fluid Mech.* **50,** 133–160.

KLINE, S. J., REYNOLDS, W. C., SCHRAUB, F. A. & RUNSTANDLER, P. W. 1967 The structure of turbulent boundary layers. *J. Fluid Mech.* **70,** 741–773.

MOFFAT, R. J. 1990 Experimental heat transfer. *Proceedings of the Ninth International Heat Transfer Conference* (Edited by HETSRONI, G.), Vol. 1, pp. 187–205. Hemisphere, New York.

MURRAY, D. B. & FITZPATRICK, J. A. 1991 Heat transfer in a staggered tube array for a gas–solid suspension flow. *Trans. ASME, J. Heat Transfer* **113,** 865–873.

OLDAKER, D. K. & TIEDERMAN, W. G. 1977 Spatial structure of the viscous sublayer in drag-reducing channel flows. *Phys. Fluids* **20,** S133–144.

PEDINOTTI, S., MARIOTTI, G. & BANERJEE, S. 1992 Direct numerical simulation of particle behaviour in the wall region of turbulent flows in horizontal channels. *Int. J. Multiphase Flow* **18,** 927–941.

PLASS, L. & MOLERUS, O. 1974 Simultane Wärmeübergangs-und Druckverlustmessungen an Feststoff/Flüssigkeits-Suspensionen im Übergansbereich vom homogenen zum heterogenen Suspensions-transport. *Chem. Ing. Tech.* **46,** 355.

RASHIDI, M. & BANERJEE, S. 1988 Turbulence structure in free surface channel flows. *Phys. Fluids* **31,** 2491–2503.

RASHIDI, M. & BANERJEE, S. 1990 Streak characteristics and behavior near wall and interface in open channel flows. *J. Fluids Engng* **112,** 164–170.

RASHIDI, M., HETSRONI, G. & BANERJEE, S. 1990 Particle–turbulence interaction in a boundary layer. *Int. J. Multiphase Flow* **16,** 935–949.

ROBINSON, S. K. 1991 Coherent motions in the turbulent boundary layer. *A. Rev. Fluid Mech.* **23,** 601–639.

ROGERS, C. B. & EATON, J. K. 1989 The interaction between dispersed particles and fluid turbulence in a flat plate turbulent boundary layer in air. Report MD-52, Stanford University, CA.

SIMONICH, J. C. & MOFFAT, R. J. 1982 New technique for mapping heat transfer coefficient contours. *Rev. Sci. Instrum.* **53,** 678–683.

SMITH, C. R. & METZLER, S. P. 1983 The characteristics of low-speed streaks in the near-wall region of a turbulent boundary layer. *J. Fluid Mech.* **129,** 27–54.

SUMER, B. M. & DEIGAARD, R. 1981 Particle motions near the bottom in turbulent flow in an open channel: Part 2. *J. Fluid Mech.* **109,** 311–337.

TSUJI, Y. 1991 Review: Turbulence modifications in fluid-solid flows. *First Joint Conference, ASME–JSME Fluids Engineering*, Portland, OR.

WILKINSON, G. T. & NORMAN, J. R. 1967 Heat transfer to a suspension of solids in a gas. *Trans. Int. Chem. Engng* **45,** 314–318.

YUNG, B. P. K., MERRY, H. & BOTT, T. R. 1989 The role of turbulent bursts in particle re-entrainment in aqueous systems. *Chem. Engng Sci.* **44,** 872–882.

ZISSELMAR, R. & MOLERUS, O. 1979 Investigation of solid-liquid pipe flow with regard to turbulence modification. *Chem. Engng J.* **18,** 233–239.

APPENDIX

Frequency Response

We estimate the frequency response of the infrared measurements. For this purpose we use a simplified model of the heater (figure A1), and solve the transient heat conduction problem:

$$\text{constantan film: } \lambda_c \frac{\partial^2 T_C}{\partial x^2} + q_v = C_c \rho_C \frac{\partial T_C}{\partial \tau} \qquad [A1]$$

$$\text{black paint layer: } \lambda_B \frac{\partial^2 T_B}{\partial x^2} = C_B \rho_B \frac{\partial T_B}{\partial \tau} \qquad [A2]$$

The boundary conditions of the two layers are given by:

$$-\lambda_C \frac{\partial T_C}{\partial x}\bigg|_{x=\delta_2} = \alpha_L (1 + \epsilon \cos 2\pi f \tau)[T_C(\delta_2) - T_L]$$

$$\lambda_B \frac{\partial T_B}{\partial x}\bigg|_{x=0} = \alpha_a (T_B(0) - T_a)$$

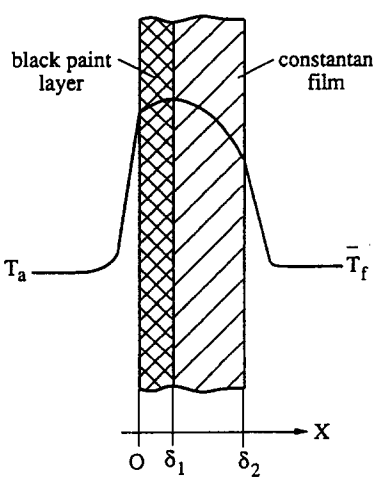

Figure A1. Simplified thermal model of the heater.

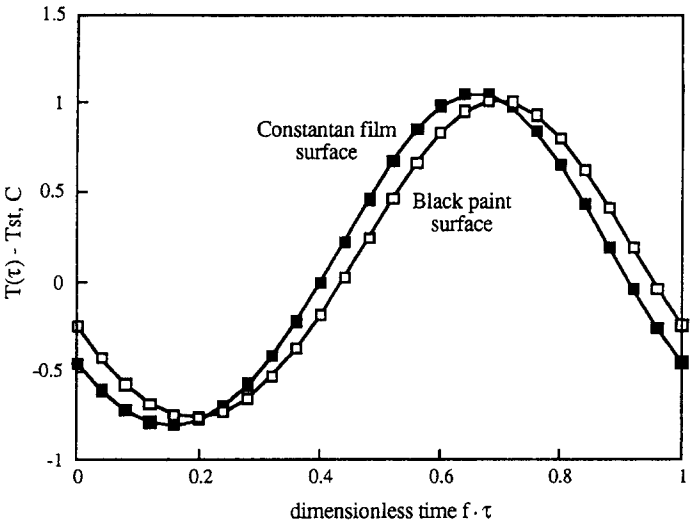

Figure A2. Solutions of the heat conduction problem for the surface temperature fluctuations at $f = 10$ Hz depending on the dimensionless time $f \cdot \tau$.

$$\lambda_c \left.\frac{\partial T_C}{\partial x}\right|_{x=\delta_1} = \lambda_B \left.\frac{\partial T_B}{\partial x}\right|_{x=\delta_1}$$

$$T_C|_{\tau=0} = T_B|_{\tau=0} = T_o \quad T_C|_{x=\delta_1} = T_B|_{x=\delta_1} \qquad [A3]$$

where T_C and T_B are the temperatures of the constantan foil and the black paint, respectively, λ are the thermal conductivities, C are the specific heats, ρ are the densities, α_L and α_a are the convective heat transfer coefficients on the liquid side and the airside, respectively, ϵ is the amplitude of the forcing function, f is the frequency of the forcing function, τ is the time and q_v is the volumetric heat generation rate. T_L and T_a are the temperature of the liquid and air, respectively.

This problem was solved numerically. Examples of the solutions for the surface temperature fluctuations $(T_B - T_{B\cdot st})|_{x=0}$ and $(T_C - T_{C\cdot st})_{x=\delta_2}$ (here $T_{B\cdot st}$ and T_{Cst} are the temperatures of the

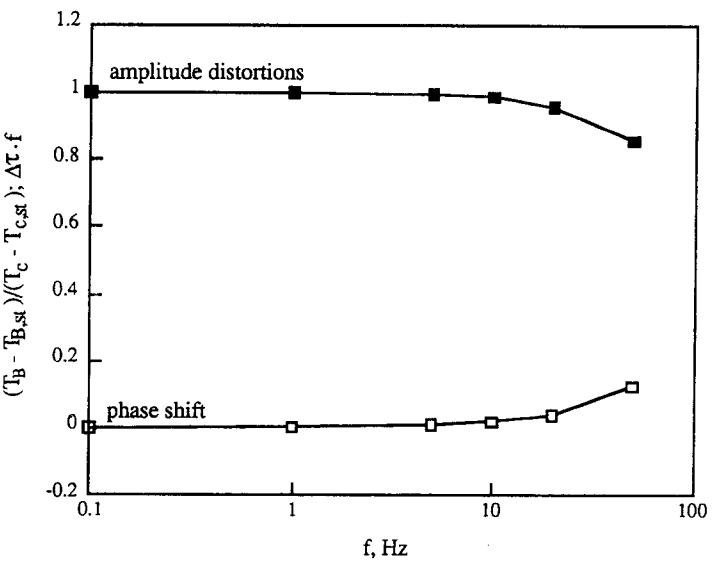

Figure A3. Values of maximal distortions of the amplitude $(T_B - T_{B\cdot st})/(T_c - T_{c\cdot st})$ and the phase shift $\Delta\tau \cdot f$ vs frequency.

black paint and the heater surface, respectively, when there is no forcing function, i.e. when $\epsilon = 0$) at $f = 10$ Hz, depending on a dimensionless time $f \cdot \tau$, are shown in figure A2 for the values:

$$\alpha_L = 1350 \text{ W/m}^2\text{C}, \ \epsilon = 0.25; \ q_v = 2.0 \times 10^{12} \text{ W/m}^3;$$

$$T_0 = 20°\text{C}; \ \delta_1 = 20 \ \mu\text{m}; \ \delta_2 = 50 \ \mu\text{m}.$$

It can be observed that there is a non-significant temperature shift of the mean temperatures of the heater sides $\Delta T_{st} = 0.123°\text{C}$.

The results of similar computations for various frequencies are shown in figure A3. It can be seen that some distortion of the temperature fluctuations begin at $f = 15 \div 20$ Hz.